Article

Estimating Thermal Material Properties Using Solar Loading Lock-in Thermography

Samuel Klein [1,*], Henrique Fernandes [2] and Hans-Georg Herrmann [1,3]

1   Chair for Lightweight Systems, Saarland University, Campus E3 1, 66123 Saarbrücken, Germany; hans-georg.herrmann@izfp.fraunhofer.de
2   Faculty of Computing, Federal University of Uberlandia, Uberlandia 38408-100, Brazil; henrique.fernandes@ufu.br
3   Fraunhofer Institute for Nondestructive Testing IZFP, Campus E3 1, 66123 Saarbrücken, Germany
*   Correspondence: samuel.klein@uni-saarland.de

Featured Application: Thermographic monitoring of a retaining wall structure.

Abstract: This work investigates the application of lock-in thermography approach for solar loading thermography applications. In conventional lock-in thermography, a specimen is subjected to a periodically changing heat flux. This heat flux usually enters the specimen in one of three ways: by a point source, a line source or an extended source (area source). Calculations based on area sources are particularly well suited to adapt to solar loading thermography, because most natural heat sources and heat sinks can be approximated to be homogenously extended over a certain region of interest. This is of particular interest because natural heat phenomena cover a large area, which makes this method suitable for measuring large-scale samples. This work investigates how the extended source approximation formulas for determining thermally thick and thermally thin material properties can be used in a naturally excited setup, shows possible error sources, and gives quantitative results for estimating thermal effusivity of a retaining wall structure. It shows that this method can be used on large-scale structures that are subject to natural outside heating phenomena.

Keywords: infrared thermography; solar loading thermography; lock-in thermography; passive thermography; thermal thickness; thermal effusivity; infrastructure; NDT

1. Introduction

The estimation of thermal material properties like effusivity of large structures poses a challenge to conventional non-destructive testing (NDT) methods. Especially active thermography reaches a technical limit when faced with measuring large-scale structures because exciting such a structure thermally is logistically hard. This article shows a method of how a quantitative estimation algorithm can be constructed and shows first results using only naturally occurring heat sources.

Currently thermal material properties like diffusivity are measured using an active setup, where the experiment conductor actively controls the excitation source. Small-scale samples can be measured via a simple heating plate setup [1]. For bigger specimen a laser-excited setup is described in [2]. Both these approaches are infeasible for a large-scale application like the retaining wall investigated in this work.

Solar loading lock-in thermography is a recently introduced measuring method and is preferable because it is particularly easy to set up. As the primary excitement period is the day-night-cycle, the measurement depth is large compared to conventional, lab-scale lock-in thermography. The thermal wavelength for a periodically excited specimen Λ is proportional to the square root of the excitation period. This thermal wavelength is the depth in which a full temperature cycle is completed. It is generally considered as the measurement depth. In addition, the measurement region can be larger than ordinary

active thermography setups would be able to excite properly. Measuring very large structures at once is possible. This is particularly interesting for monitoring buildings and large infrastructure alike. This work focuses on large vertical, thermally thick (d > Λ) structures. Multiple assumptions and approximations were made to use the theoretical lock-in thermography formulas on solar loading thermography data. These assumptions result in systematic error. Later a calibration method will be shown, that eliminates any linear errors that were made, by means of a calibration against known material property values.

Related work shows that this method can be successfully used for detecting defects and characterize their depths [3]. Other related work focusses on the time when the sun is obstructed, and a shadow is cast, triggering the thermal camera to begin a pulse-phase-thermography (PPT) measurement [4]. For this work these exact requirements of shadow cast are not needed. Instead, this work specifically choses the 24 h period to suppress transient effects (like cloud shadows or short-term weather effects like gusts of wind) and generate results dependent only of the much slower 24 h excitation intensity. Furthermore, only qualitative results have been shown (i.e., cracks or delaminations) and not quantitative measurements of material properties. This has the benefit of not only being able to detect defects, but also characterize the material under test.

2. Materials and Methods

This work uses two reference plates made out of EN AW 5083 aluminum sized $300 \times 300 \times 10$ mm and $300 \times 300 \times 20$ mm respectively. Using literature values for the thermal material properties described by [5] $\varrho = 2660$ kg/m^3, $\lambda = 125$ W/(m $\cdot$ K), $c_p = 900$ J/(kg $\cdot$ K) results in thermal masses of 2106 J/K and 4212 J/K respectively.

A concrete block was fabricated out of premixed dry mortar with a size of $300 \times 300 \times 300$ mm to be used as a thermally thick reference. Material properties were assumed to be [6] $\varrho = 2240$ kg/m^3, $\lambda = 2$ W/(m $\cdot$ K), $c_p = 900$ J/(kg $\cdot$ K), resulting in a thermal effusivity of $b_{conc} = 2008$ J/$\left(\text{K} \cdot \text{m}^2 \cdot \sqrt{\text{s}}\right)$.

The brickwork measured in the field experiment is assumed to have the following thermal properties [6]: $\varrho = 1920$ kg/m^3, $\lambda = 0.9$ W/(m $\cdot$ K), $c_p = 800$ J/(kg $\cdot$ K), resulting in a thermal effusivity of $b_{brick} = 1176$ J/$\left(\text{K} \cdot \text{m}^2 \cdot \sqrt{\text{s}}\right)$. The retaining wall itself is approx. 8 m tall and extends laterally over 100 m, of which a single measurement site of approx. 4 m by 4 m was chosen.

A custom measurement platform was developed, powered by a rechargeable battery and consisting of an embedded Linux single board computer (RaspberryPi 3B) and the FLIR Boson 640 in USB Video (UVC) mode. The FLIR Boson LWIR camera can directly send raw image data over USB, which was used in all further processing. Thermal simulations were carried out using GNU Octave and MATLAB.

3. Theoretical Framework

Solar loading lock-in thermography uses no artificial heat source, like heat lamps, but only naturally occurring heat sources. These consist of the following: Heat transfer within the structure (conduction). Heat transfer with the surrounding air, which is free to move (convection) and heat transfer via radiation (solar irradiation, radiative heat loss). The fourth heat source, evaporative cooling, is neglected in this work.

Conduction within a static material is a linear process $\sim \Delta T$, governed by the heat equation. Natural convection is a non-linear process that is commonly linearized by defining an "overall heat transfer coefficient" [6], convection in a natural setting, where ambient temperatures, humidity and air speeds are always changing is very hard to accurately represent in a single coefficient. Thermal radiation is a major non-linear process $\sim T^4$ that may be linearized for a single temperature region. The accuracy of thermal radiation linearization is discussed later in more detail.

To estimate thermal material properties the value of the heat input density amplitude (irradiance) of a periodic excitation is needed. The heat input is also assumed to be periodic and sinusoidal.

Estimating the heat input that occurs in a specific frequency content of the total excitation is inaccurate. Especially for overcast days, and frequencies higher than 1/24 h direct measurements are necessary. One way of measuring the heat input is a measuring solar irradiance (e.g., via a pyranometer). Another way of determining heat input, presented in this work, is done by placing thermally known reference samples into the measurement setup and using the thermal response of the reference samples to infer the preceding irradiation amplitude in frequency domain. Subsequently using formulas from lock-in thermography to determine the heat flow amplitude, which in turn arise from the heat equation using various assumptions and simplifications.

The thermal imaging long wave infrared (LWIR) camera is set up in a fixed manner to capture a set of thermal images that are regularly spaced in time. These images represent a 2D temperature field that is assumed to accurately depict the surface temperature of the captured structure. Thermal imaging cameras can be calibrated and adjusted to radiation to measure more accurate results [7]. A two-point calibration with a calibration radiator is performed within the approximate temperature range to get temperature estimates as close to the real temperature as possible. Other effects, like emissivity/reflectivity can be corrected as well to further improve absolute measuring accuracy for a given surface. These kinds of corrections were not performed in the scope of this work but are hypothesized to further increase measurement accuracy.

A time series matrix is arranged from the temperature field T_{xy}, which is called T_{xyt} with the third dimension being time. The time series for each pixel is then transformed into frequency domain by multiplying with the complex frequency ω in time. This is similar to using a lock-in amplifier. The main difference is that the reference oscillator is generated inside the Fast Fourier Transform (FFT) and never subject to any feedback from the signal itself. Therefore, two main conditions have to be met to ensure the error being as low as possible.

(1) For the fundamental frequency and its respective harmonics amplitudes to result in a single bin, the measurement time shall be an exact multiple of the fundamental interval (in this work 24 h).
(2) The local start time of the measurement is captured because it defines the reference Phase value, each calculated phase is related to.

The resulting matrix $S_{xy}(\omega)$ contains the complex coefficients describing either amplitude/phase or real/imaginary (often called $0°/90°$) components for each pixel of the image [8].

The reference signal of a conventional lock-in amplification method is generated inherently and is available for the lock-in transform algorithm by design [8]. However, in ambient thermography, the reference signal is generated artificially. A pure sinusoidal signal $ref_t(\omega) = \hat{e}(-i\omega t)$ is used as the reference. Note that this is a set of vectors in time for each frequency considered:

$$S_{xy}(\omega) = \sum_t T_{xyt} \cdot ref_t(\omega)$$

The amplitude of S_{xy} is of particular interest because it depicts the amount of temperature change the surface has undergone at a particular frequency. Under simplified conditions, these amplitudes are directly related to material properties. Table 1 summarizes these relations in a table.

Table 1. Real and imaginary part of the temperature signal from [8] (p.120).

Thermal Thickness	$\Re\{S_{xy}\}$	$\Im\{S_{xy}\}$
Thermally thin	0	$\frac{p}{\rho d c_p \omega}$
Thermally thick	$\frac{p}{\sqrt{2\omega\lambda\rho c_p}}$	$\frac{p}{\sqrt{2\omega\lambda\rho c_p}}$

Excerpt of the table: p Thermal flux density; λ Thermal conductivity; ω Angular excitation frequency; c_p Specific thermal capacity; ρ Mass density.

Thermal effusivity is defined as $b = \sqrt{\lambda \rho c_p}$. Substitution leads to:

$$b = \frac{p}{|S_{xy}| \cdot \sqrt{\omega}} \tag{1}$$

A three-step method is devised, that estimates the thermal effusivity of every pixel in the scene:

(1) Place a reference sample inside the measured frame with known material properties to get an approximation of p. From Table 1 we get:

$$p = |S_{xy}| \cdot \rho d c_p \omega \tag{2}$$

Note that this is only valid for thermally thin samples.

(2) Empirically correct p to better approximate the input power density amplitude that the actual body is subjected to:

$$p_{eq} = p \cdot c(\omega) \tag{3}$$

where $c(\omega)$ is an empirical function that is determined by linear regression.

(3) Approximate thermal effusivity b by inserting p_{eq} into Equation (1). This results in the final formula:

$$b_{corr} = \frac{p \cdot c(\omega)}{|S_{xy}| \cdot \sqrt{\omega}} \tag{4}$$

The approximation of p via the reference body can only be applied to estimate b if it is used on a part of the surface that is indeed thermally thick. Additionally, approximating heat flow to be linear in relation to input power is detrimental to the accuracy if thermal radiation to the surroundings contributes to a significant part of heat transferred. Thermal radiation heat transfer is in general of the form $p_{rad} \propto T_{obj}^4 - T_{amb}^4$ and can be estimated linearly only for small amplitudes in object and ambient temperature. Simple thermal mass point simulations show that the radiative heat loss accounts for an approximatively constant part of the overall heat loss in respect with excitation strength. Linearizing radiative heat loss within naturally occurring temperatures (0 °C to 40 °C) results in a maximum error of 2.4% percent, which is less than many other approximating factors that were assumed earlier.

On empirically correcting the results: One of the biggest error terms is that the real heat input density in the field experiments is unknown. Especially heat loss via convection and radiation is hard to determine directly as it is dependent on multiple significant factors that were listed above. In a first approach to measuring thermal material properties using solar loading thermography, a regression method is used to match the measured results to the literature value of a specific material (in this case brick and concrete).

Other error sources include but are not limited to:

(1) Temperature distribution in thick materials is dispersive, because thermal material properties like thermal conductivity often depend on the temperature itself.
(2) Heat radiation estimations should consider the temperature distribution of the half space and not estimate the ambient radiation temperature to be constant, especially at nighttime with clear skies, the sky heat sink is significant. The black body temperature T_{amb} of the night sky ranges between −40 °C and −10 °C [9].

To validate the proposed algorithm the following steps were carried out:

(1) Thermal simulations with an idealized setup to validate the theoretical formulas and assess the impact of convective and radiative heat loss.

(2)　Laboratory experiments with an artificial infrared heating source and thermally thin (two aluminum plates) and thick (one concrete block) samples being heated from one side in a periodic manner.

(3)　A field experiment on a vertical retaining wall. It consists of a combination of brick, mortar, plastering and concrete with varying depths of each of these materials.

4. Results and Discussion

4.1. Thermal Simulations

Multiple transient thermal simulations were carried out to validate the theoretical formulas. The aluminum reference plates were simulated by a mass point with a thermal mass of $m_{th} = \rho V c_p$ each, subjected to a periodic heat input, as well as to convective and radiative cooling.

Convective cooling is assumed to be linear in respect to temperature difference and uses a free convection rate of $5\,\text{W}/(\text{m}^2\text{K})$ for all specimen. Radiative cooling was simulated using a constant ambient temperature of 21 °C and emissivity of $\varepsilon = 1.00$ for all specimen, to simplify radiation calculations.

The simulation results, shown in Figure 1, correlate well with the analytical results according to Equations (1) and (2). For greater heat input amplitudes, the simulation temperature amplitude is lower than expected, as the theoretical formulas do not take the cooling effects into account. Overall, a good correlation is shown for common solar irradiance values ($<1200\,\text{W}/\text{m}^2$). Moreover, non-linear effects are negligible.
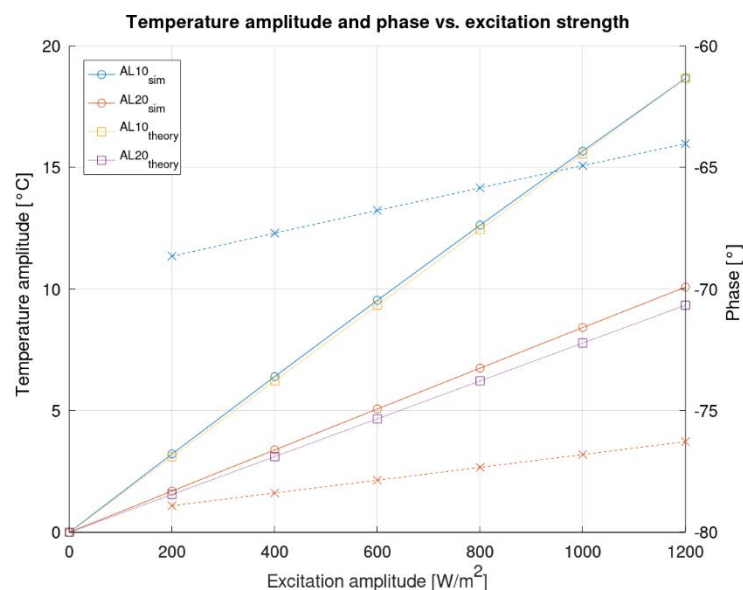

Figure 1. Amplitude and phase angle of the temperature signal from the thermal simulation in comparison to the analytical formula (cf. Equations (1) and (2)). The dotted line shows the phase angle and the solid line the temperature amplitude. Depicted here are temperature amplitudes and phase angles calculated by the FFT in relation to heat input density.

4.2. Laboratory Experiments

In the indoor laboratory experiments, the two reference plates, described in Section 1, were set up vertically on a desk, together with the concrete cube and subjected to an infrared heating lamp, controlled by a computer. The laboratory setup and a sample thermogram is shown in Figure 2.
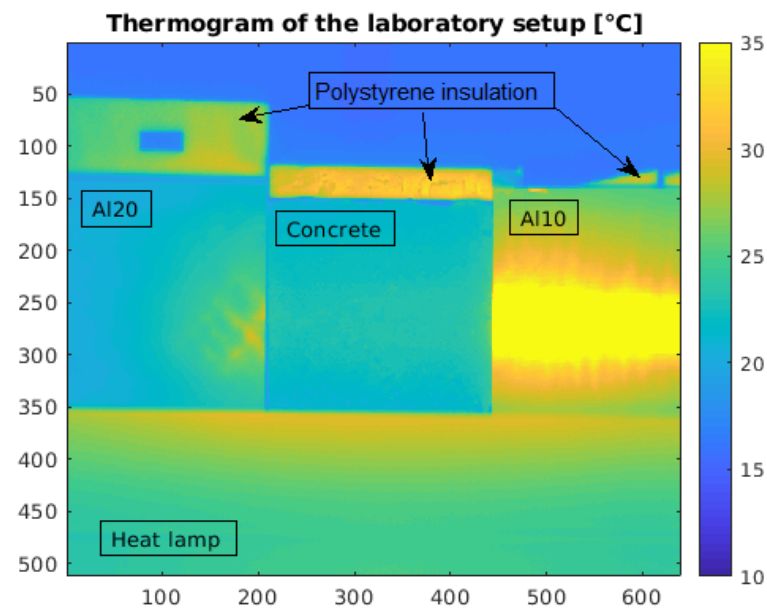
Figure 2. Overview of the laboratory setup. Note the polystyrene insulation in the back of each sample to ensure the backside only experiences minor heat loss.

The periodic heating signal was varied so that a periodic square wave excitation was generated, which in turn could be varied in period. The heat lamp is a 3000 W infrared lamp for sauna application laid horizontal on a desk with a distance of approx. 60 cm to the subjects under test. This results in a maximum irradiation of 800 W/m^2.

This setup was specifically chosen to test the proposed algorithm by having both thermally thick and thermally thin test samples in one setup, to infer information from the reference plates to the concrete block. The excitation periods were: 90, 45, 22.5, 11.25, 5.625 and 2.8125 min.

The upper limit of the excitation period is determined by the thickness of the thermally thick reference body (concrete cube block) that has a side length of 30 cm. The resulting maximum excitation period is ~90 min, as the corresponding thermal wavelength Λ is almost 30 cm. Reflections from the backside of the specimen will become non-negligible if the excitation period were to be extended (the thermally thick reference block would no longer be thermally thick).

Further work could either test outside on a thermally thick wall, construct a larger reference body, or choose a material with a lower effusivity. The latter effectively shortens the thermal wave length. However, due to the increasing effect of environmental effects for materials with lower effusivity, this has the drawback of higher error.

Additionally, in the laboratory setup concrete was chosen as a reference material, because it is much easier to fabricate homogenous block of any size than with brickwork. Using fabricated brickwork here however, would allow a direct comparison of the laboratory experiments and field experiment effusivity value.

The laboratory experiments, depicted in Figure 3, show good correlation in the lower excitation period range with less correlation on longer periods. These result in longer timespans, in which cooling effects are active. In addition, non-linear cooling effects (like radiative cooling) are more pronounced because the specimen heats up more than in experiments with shorter periods. Furthermore, the square root dependency of the thermally thick concrete block temperature amplitude is depicted well (green line with approx. half the slope of the other curves).
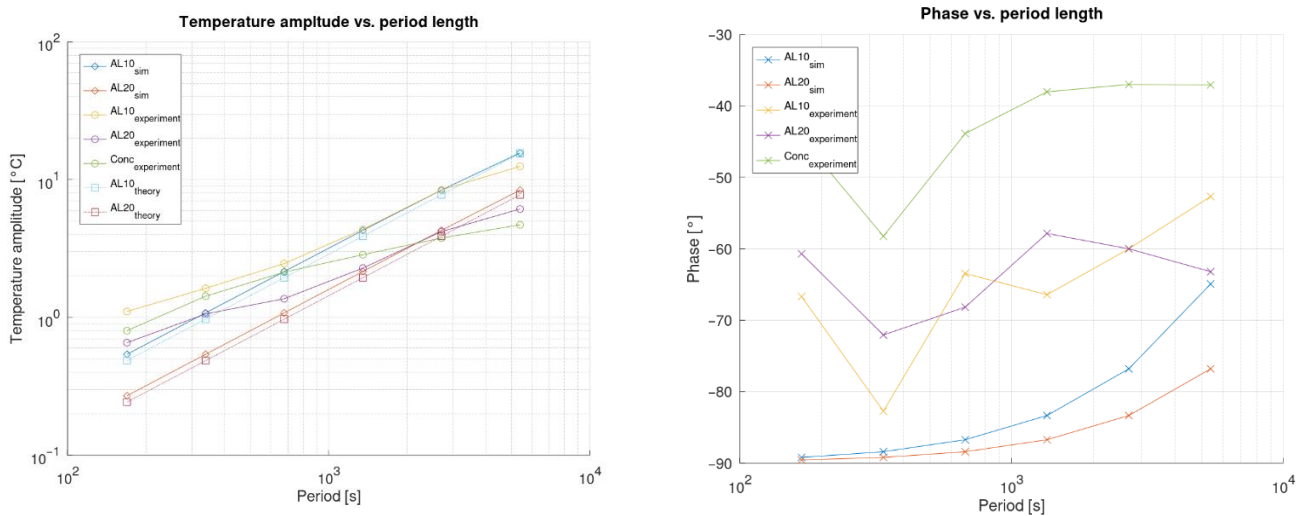
Figure 3. Amplitude and phase angle of the temperature signal from the thermal simulation and laboratory experiments and analytical solution. Depicted here are temperature amplitudes and phase angles calculated by the FFT in relation to excitation period. Note the theoretical phase angle for thermally thin and thick materials is −90° and −45° respectively.

The experimental laboratory results point to greater inaccuracies with longer periods, indicating a poor correlation between theoretical formula and real value in 24 h periods (ultimately used in this work). Therefore, an empirically determined correction factor was introduced to correct these aforementioned errors.

This approximation factor was calculated using a regression function on the various data points collected by means of laboratory experiments and field experiments. In the experiments, the correction factor $c(\omega)$ was calculated using the following equation:

$$c(\omega) = \frac{b_{literature}}{b(\omega)} \tag{5}$$

where b is calculated from Equation (3). The literature value for the concrete sample block is $2000 \, \mathrm{J}/\left(\mathrm{K} \cdot \mathrm{m}^2 \cdot \mathrm{s}^{1/2}\right)$ [6] (p. 717). The effusivity of the wall structure was assumed to be $1000 \, \mathrm{J}/\left(\mathrm{K} \cdot \mathrm{m}^2 \cdot \mathrm{s}^{1/2}\right)$ (Effusivity of brick [6] (p. 716)). Determining the correction factor for each excitation period results in a point plot, which was fitted by a linear function shown in Figure 4.
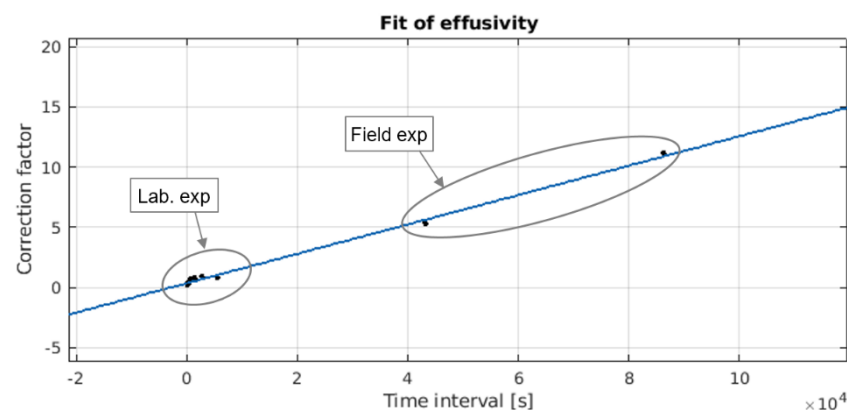

Figure 4. Plot of the correction factors determined by the method depicted above. Note that the shorter time periods were determined in the laboratory experiments and the 24 h and 12 h correction factor was determined in the field experiment.

This correction factor compensates for all systematic errors that rose during simplification but has the limitation that it cannot correct for non-linear errors.

4.3. Field Experiments

The LWIR camera was set up in a fixed manner with approximately 9.5 m distance to the wall. Thermal images were captured for 96 h. The wall under investigation, positioning of the ROIs and a typical thermogram are depicted in Figures 5–7.

Figure 5. Overview of the wall structure under test. The rectangle shows the approximate view of the LWIR camera.
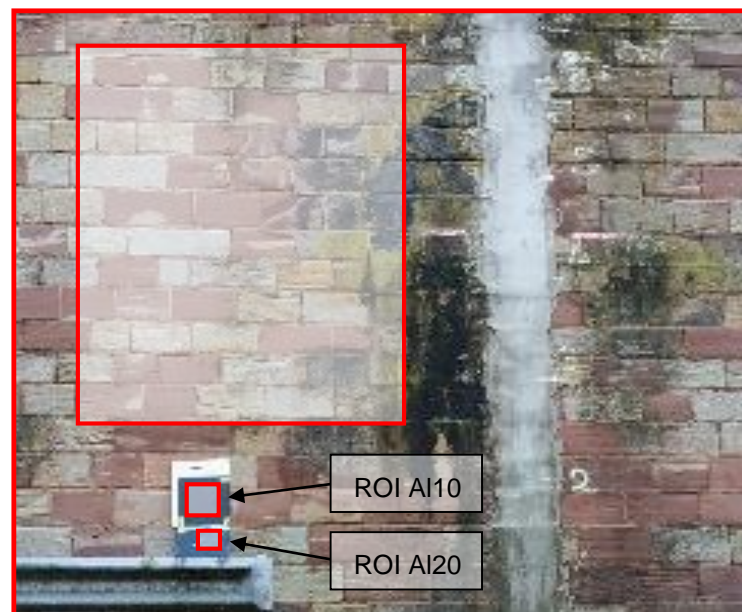
Figure 6. ROI location and size. In the lower left are the two reference plates (aluminum plates, each 300 × 300 mm size, one 10 mm, the other 20 mm thick). On the right side, a plaster strip is visible from earlier experiments on the wall.
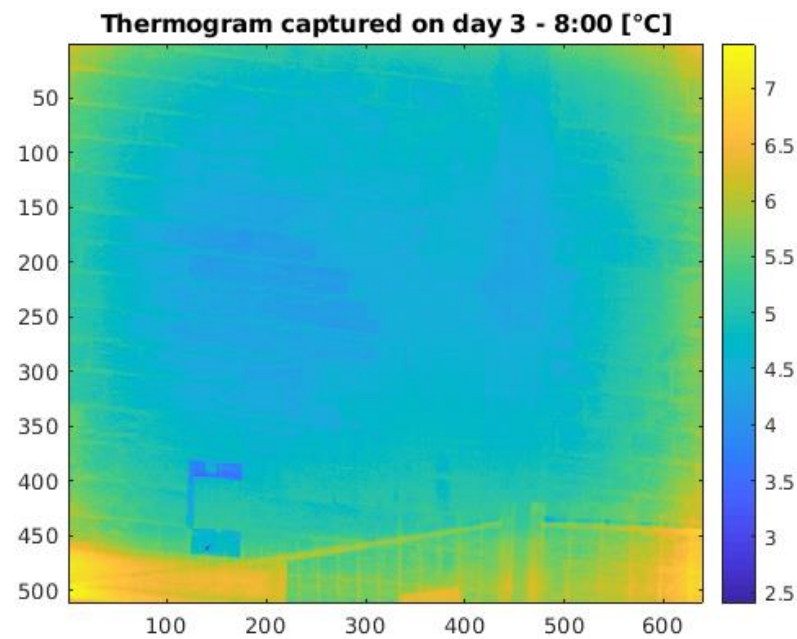
Figure 7. Typical thermogram showing the retaining wall. In the lower left are the two reference plates stacked on top of each other. Note the vignetting effect on the cameras lens has not been fully corrected. However, for the proposed algorithm, this correction is not necessary.

Figure 8 shows the time series values for the three evaluated ROIs over the measurement period. This data shows very poor 24 h period amplitude. This is due to the weather being overcast for almost the whole time (see Table 2). The algorithm (Equation (4)) was evaluated on this data set. Even better results are expected on days with strong sun, and no overcasts to disturb the periodic heat input, also advised by [10]. The amplitude image, shown in Figure 9, is calculated and from these amplitudes the effusivity is estimated and depicted in Figure 10.
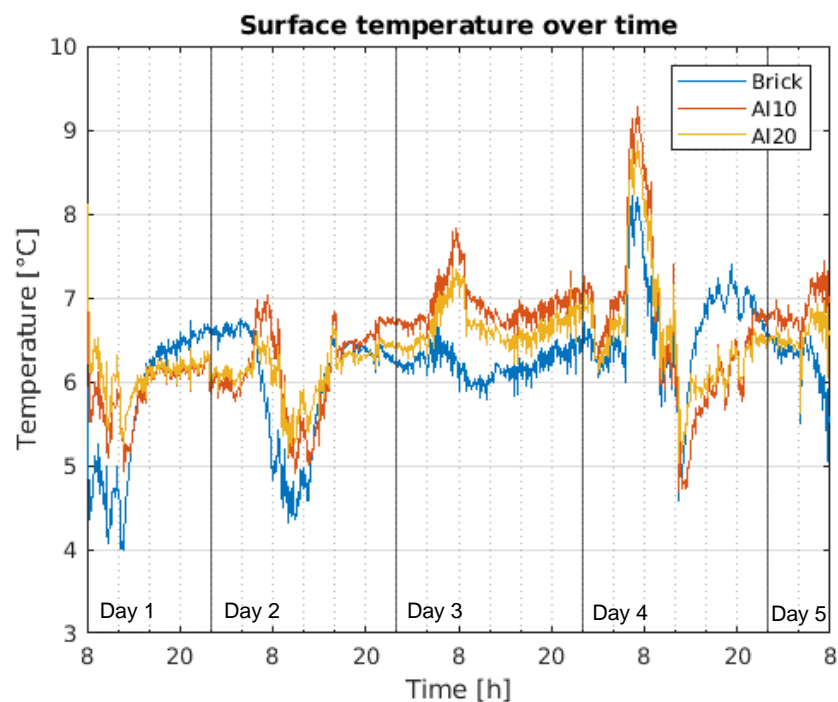
Figure 8. Average surface temperature for the ROIs depicted above. Noticeable is the greater temperature difference of the Al10 plate vs the Al20 plate, caused by the lower thermal mass.

Table 2. Weather table for the 96 h experiment. Weather data is collected by [11] for the weather station "Saarbrücken-Ensheim" which is located ~11 km from the experiment site. Note the high average cloud coverage and low total sunshine per day.

Day	Date	Min. Temp. [°C]	Avg. Temp. [°C]	Max. Temp. [°C]	Total Sunshine [h]	Avg. Humidity [%RH]	Total Rain [mm]	Cloud Coverage [%]
1	9 November 2020	−0.3	3.2	7.0	0.5	93.2	1.1	70
2	10 November 2020	−1.2	0.7	3.0	0.6	96.3	0.0	70
3	11 November 2020	0.6	2.8	4.5	0.0	94.3	2.9	98
4	12 November 2020	0.9	4.2	7.8	1.5	85.1	0.3	78
5	13 November 2020	0.8	2.7	4.2	0.0	94.6	0.5	98
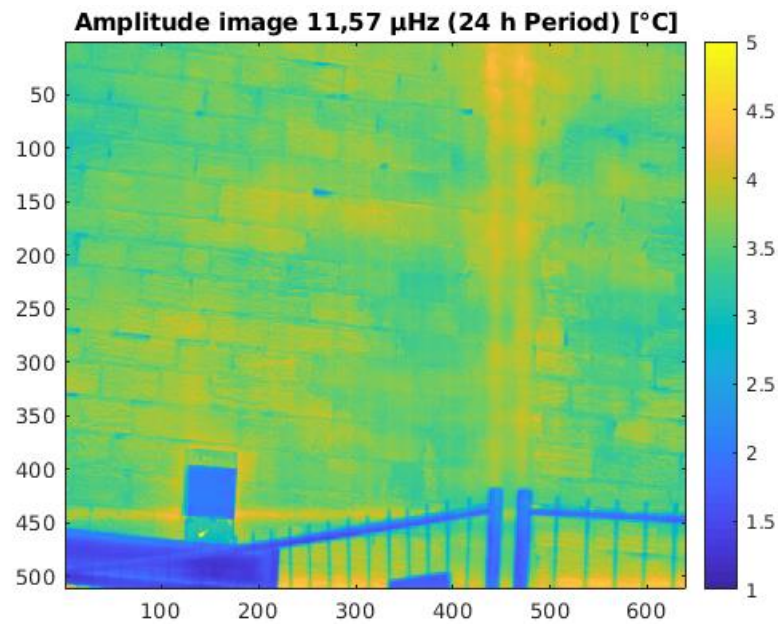
Figure 9. Amplitude image of the fundamental 24 h period. This image depicts the 24 h temperature amplitude average in every pixel over the 96 h measurement period $|S_{xy}|$.
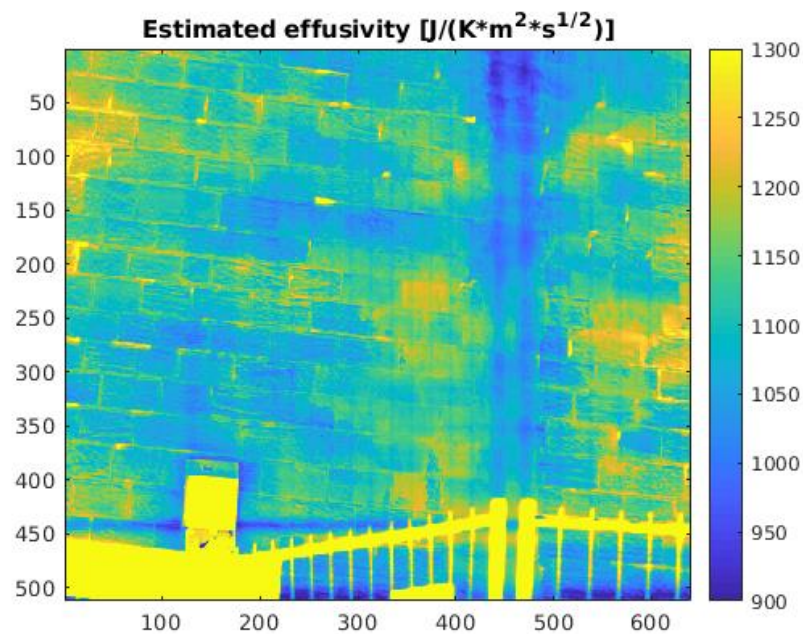

Figure 10. Estimated thermal effusivity for each pixel. Note that these results are only valid for regions that are thermally thick. Regions like the reference plates or the steel fence result in meaningless effusivity values.

There are two regions with higher and lower apparent effusivity of particular interest:

- The gaps between bricks (made out of an unknown type of mortar) correctly measure higher values than the bricks themselves
- The plaster strip on the right correctly measures lower effusivity than brick (plaster ~900 vs. brick ~1100 $J/\left(K \cdot m^2 \cdot s^{1/2}\right)$). Note that the plaster strip is strictly speaking not thermally thick. However, as the sensitivity of the measured effusivity is greatest in the front and less sensitive to the back layers the result correlate well to literature values for these materials. This sensitivity drop along the z-axis stems from the fact that the temperature amplitude of the structure drops exponentially over the depth [8]. Experiencing less amplitude, deep layers cannot influence the surface temperature as much as the front layers. Exact estimations on which layer has how much impact is not fully examined yet.

Phase Evaluation and Thermal Thickness

In theory, thermally thin materials show a negative 90-degree angle relative to the excitation. This makes intuitive sense, because the temperature of the material will rise until the excitation reaches zero again. After which the temperature of the object begins to fall. Thermally thick materials should show negative 45-degrees. This is because internal heat transfer is not negligible and changes how the surface reacts to heat input. These phase angle differences between thermally thick and thin materials are present in laboratory as well as field experiments. The experimental phase angle difference in the laboratory setup is ~30 degrees and in the field ~60 degrees. In both cases using the fundamental excitation frequency, based on phase evaluation the correct objects in frame are identifiable as thermally thick or thin. It is hypothesized that the phase angle information can be used to determine "thermal thickness" or at the very least to distinguish thick from thin in thermally adequate circumstances. Former research shows that phase evaluation is a valid method to identify subsurface defects or material changes [11,12]. This confirms the hypothesis and may contribute a factor to explaining their findings.

In the field experiments, thermal thickness can be inferred correctly from phase angle images, depicted in Figure 11. Figure 5 shows how the reference plates, the guardrail in the lower left corner and the construction fence in the lower part of the image significantly differ in their phase angle compared to the thermally thick retaining wall structure.

To what extent this method generally can be used to determine apparent thermal thickness is subject to ongoing research. What certainly is known that determining other thermal material properties using phase information, like thermal effusivity, thermal conductivity and alike, is much harder, because the phase angle depends on other variables more strongly than solely thermal material properties [11].

Especially excitation variation (over multiple days) will result in phase angle shifts.
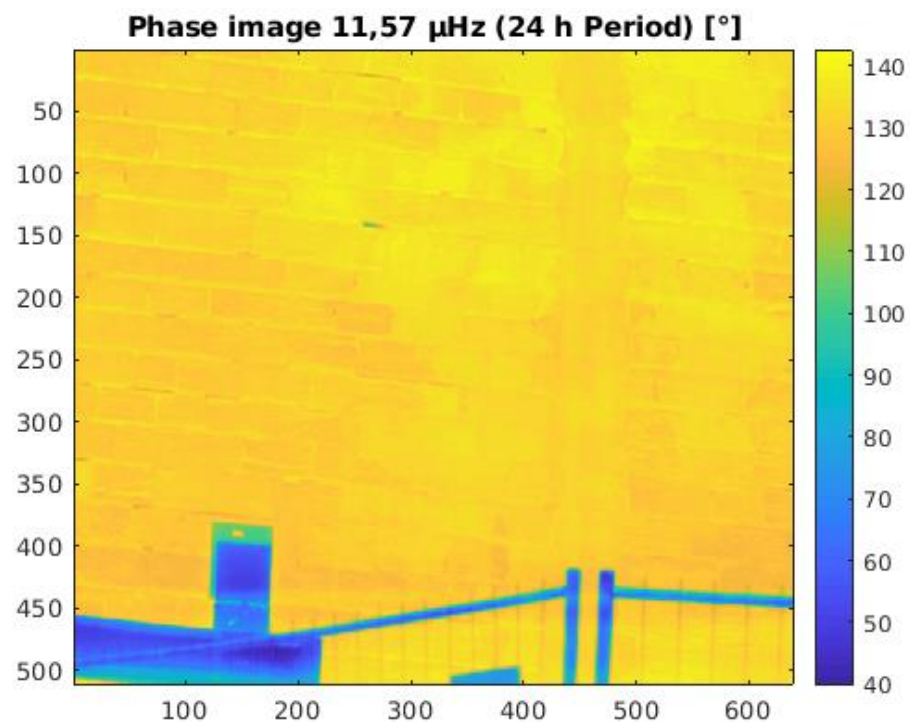
Figure 11. Phase image of the fundamental 24 h period. This image depicts the 24 h phase information every pixel over the 96 h measurement period $arctan\left(\Im m\{S_{xy}\}/\Re e\{S_{xy}\}\right)$. Note that 90° phase would correlate to an angle of a sine wave, which has its origin at the time of the experiment start (8:00) and maximum 6 h later at 14:00. Note that higher angle values mean 'earlier' thermal responses to the input. If the phase angle value is lower, that corresponds to a 'slower' response to the periodic heat input.

5. Conclusions and Further Work

The presented algorithm has shown good measurement results, albeit non-optimal measurement conditions in the field experiment. It can not only obtain qualitative measurement results on the retaining wall structure but also identify thermal thickness differences using the phase angle information. The application of the presented algorithm can be extended to other kinds of infrastructure for inspection and monitoring purposes.

Further work has to be done to bring the measured results closer to the actual thermal material properties of the structure; this involves separating thermal effects to get a better understanding on the exact heat flow acting on the test subject. How phase angle information can be used to estimate thermal thickness and do quantitative analysis in specific setups is subject to ongoing research as well.

The calibration approximation has to verified under other conditions like other materials or other excitation conditions (i.e., more Sun, another season). If the approximation and regression fit holds for the other conditions, it can be shown to be sufficiently robust to investigate further on how this exact finding can be explained considering the physical effects acting on the test subjects.

Furthermore, increasing accuracy by isolating singular systematic error sources and developing a more sophisticated correction term based on physical properties can be done. For example, measuring apparent ambient temperature with a pyrgeometer and estimating radiative heat flux directly. Using a pyranometer to measure radiative heat input the remaining heat in-/output can be inferred to be convective. Finally, all heat in- and outputs are known and a more accurate model can be set up.

Lastly, a novel method could be devised to include amplitude information from various other frequencies. This work focusses solely on the fundamental 1/24 h frequency, where as other frequency bins are sure to contain additional information.

References

1. Boué, C.; Holé, S. Infrared thermography protocol for simple measurements of thermal diffusivity and conductivity. *Infrared Phys. Technol.* **2012**, *55*, 376–379. [CrossRef]
2. Ishizaki, T.; Nagano, H. Measurement of 3D thermal diffusivity distribution with lock-in thermography and application for high thermal conductivity CFRPs. *Infrared Phys. Technol.* **2019**, *99*, 248–256. [CrossRef]
3. Sfarra, S.; Marcucci, E.; Ambrosini, D. Infrared exploration of the architectural heritage: From passive infrared thermography to hybrid infrared thermography (HIRT) approach. *Mater. Constr.* **2016**, *66*, 94. [CrossRef]
4. Krankenhagen, R.; Maierhofer, C. Pulse phase thermography for characterising large historical building façades after solar heating and shadow cast—A case study. *Q. InfraRed Thermogr. J.* **2013**, *11*, 10–28. [CrossRef]
5. EN AW 5083 Data Sheet. Available online: https://gleich.de/en/wp-content/uploads/sites/4/2016/10/en_en_aw_5083.pdf (accessed on 5 February 2021).
6. Lienhard, J.H., IV; Lienhard, J.H., V. *A Heat Transfer Textbook*; Phlogiston Press: Cambridge, MA, USA, 2020.
7. Quirin, S.; Herrmann, H.-G. Combining the spectral information of Dual-Band images to enhance contrast and reveal details. *QIRT* **2018**. [CrossRef]
8. Breitenstein, O.; Warta, W.; Langenkamp, M. *Lock-in Thermography*; Springer: Berlin/Heidelberg, Germany, 2010. [CrossRef]
9. Goforth, M.; Gilchrist, G.; Sirianni, J. Cloud effects on thermal downwelling sky radiance. *AeroSense Int. Soc. Opt. Photonics* **2002**, *4710*, 203–213. [CrossRef]
10. Bortolin, A.; Cadelano, G.; Ferrarini, G.; Bison, P.; Peron, F.; Maldague, X. High-resolution survey of buildings by lock-in IR thermography. In Proceedings of the SPIE 8705, Thermosense: Thermal Infrared Applications XXXV, 870503, Baltimore, MD, USA, 22 May 2013. [CrossRef]
11. Wetter und Klima—Deutscher Wetterdienst. Available online: https://www.dwd.de/DE/leistungen/klimadatendeutschland/klimadatendeutschland.html (accessed on 5 February 2021).
12. Ibarra-Castanedo, C.; Sfarra, S.; Klein, M.; Maldague, X. Solar loading thermography: Timelapsed thermographic survey and advanced thermographic signal processing for the inspection of civil engineering and cultural heritage structures. *Infrared Phys. Technol.* **2017**, *82*, 56–74. [CrossRef]